Evaluating Unsupervised Methods to Size and Classify Suspended Particles Using Digital In-Line Holography

Emlyn J. Davies,* Daniel Buscombe,[+] George W. Graham,[#] and W. Alex M. Nimmo-Smith

School of Marine Science and Engineering, Plymouth University, Plymouth, United Kingdom

ABSTRACT

Substantial information can be gained from digital in-line holography of marine particles, eliminating depth-of-field and focusing errors associated with standard lens-based imaging methods. However, for the technique to reach its full potential in oceanographic research, fully unsupervised (automated) methods are required for focusing, segmentation, sizing, and classification of particles. These computational challenges are the subject of this paper, in which the authors draw upon data collected using a variety of holographic systems developed at Plymouth University, United Kingdom, from a significant range of particle types, sizes, and shapes. A new method for noise reduction in reconstructed planes is found to be successful in aiding particle segmentation and sizing. The performance of an automated routine for deriving particle characteristics (and subsequent size distributions) is evaluated against equivalent size metrics obtained by a trained operative measuring grain axes on screen. The unsupervised method is found to be reliable, despite some errors resulting from over-segmentation of particles. A simple unsupervised particle classification system is developed and is capable of successfully differentiating sand grains, bubbles, and diatoms from within the surfzone. Avoiding miscounting bubbles and biological particles as sand grains enables more accurate estimates of sand concentrations and is especially important in deployments of particle monitoring instrumentation in aerated water. Perhaps the greatest potential for further development in the computational aspects of particle holography is in the area of unsupervised particle classification. The simple method proposed here provides a foundation upon which further development could lead to reliable identification of more complex particle populations, such as those containing phytoplankton, zooplankton, flocculated cohesive sediments, and oil droplets.

1. Introduction

Characterizing particles suspended in seawater has become a critical component in understanding the organic carbon cycle, ocean acidification, oceanic circulation, and future climate predictions. Possessing a method to accurately and automatically characterize these particles has therefore become important for many areas of marine science and monitoring. For example, suspended particles serve as passive tracers that aid the understanding of turbulent mixing of plankton, heat, and salinity. The measurement and understanding of suspended sediment flux is crucial for the prediction of coastal and estuarine change, the operation of ports and harbors, and the safe passage of shipping. Suspended particles also play a key role in controlling radiative transfer (therefore, the interpretation of satellite ocean color imagery) and primary productivity. Particles also scatter sound—a principle that enables acoustic measurements of flow velocities, suspended mineral sediments, and bathymetric mapping. Information on the type (organic, inorganic, photosynthesizing, non-photosynthesizing), size, shape, and concentration of particles in seawater provides the necessary insight required to advance understanding of these fundamental processes within the marine environment.

Many techniques for measuring marine particles exist, yet currently only laser diffraction and imaging are in routine use to provide in situ estimates of concentration and size distribution. Techniques based on single-frequency acoustic backscatter are currently limited to concentration only (Thorne and Hanes 2002). Multifrequency acoustics can theoretically provide both concentration and size distribution estimates (Thorne and Buckingham 2004); however, development in this area is hampered by the sensitivity of these estimates to particle shape and density (Moate and Thorne 2012). Concentration and size estimates based on laser diffraction are also affected by particle shape (Agrawal et al. 2008; Graham et al. 2012) and composition (Andrews et al. 2010). These technologies that rely on acoustical and optical scattering are affected by aeration in surface waters. In contrast, imaging systems resolve individual particles, enabling simple, calibration-free measurements of particle shape, size, and concentration. Imaging is relatively insensitive to small concentrations of bubbles (unless bubbles adhere to the optical windows). In addition, imaging is currently the only method that permits relatively easy individual particle classification. For example, images can be used to distinguish mineral particles from phytoplankton or zooplankton.

Conventional (lens based) imaging of suspended particles suffers from depth-of-field, particle occlusion and focusing issues. However, digital in-line holography promises to overcome many of these limitations (Owen and Zozulya 2000; Sheng et al. 2006; Sun et al. 2008; Graham and Nimmo-Smith 2010). With the recent introduction of commercially available submersible holography systems [to date, the Laser In Situ Scattering and Transmissivity Holographic System (LISST-Holo), by Sequoia Scientific Inc. under license from Plymouth University, and the Submersible Microscope system made by 4Deep], specifically designed to image marine particles, the use of digital in-line holography as a viable in situ method for particle measurements in marine environments is anticipated to rise (Stemmann and Boss 2012). Because of the number of steps required to retrieve particle information from holograms and the number of images recorded, manual particle extraction becomes infeasible for most datasets, creating a pressing need for automated processing that is comparable in accuracy to that available for other sizing techniques, such as laser diffraction. In complex particle populations, there is a need to distinguish between, and classify, multiple particle types (Davies et al. 2014; Zhang et al. 2014). Examples include distinguishing between zoo- and phytoplankton, or mineral or organic particles and bubbles. This paper details the computational considerations required to automatically focus and segment individual particles from a raw hologram, and then automatically size and classify these particles.

Following a brief introduction to in-line holography, we outline an improved method for holographic reconstruction that combines previously published methods with new advances in noise removal within the reconstruction process. The improved holographic processing is then used to formulate a simple and effective method for classifying particles by type. Finally, we discuss the considerations required for successful automated processing, the limitations of the current techniques, and provide suggestions for future developments.

2. Principles of in-line holography

A digital hologram (Fig. 1) records the pattern of interference between two beams: 1) a source beam of collimated laser light and 2) the source beam that has been diffracted by scattering objects (such as particles) in its path. The pattern recorded by a charge-coupled device (CCD) or a similar sensor contains information on the phase and amplitude of the diffracted wave that can be used to size and position the object that caused the scattering. For the case of scattering being caused by particles suspended in seawater, this numerical reconstruction procedure is the subject of section 4a, producing in-focus images of every particle in the sample volume, eliminating the problems associated with depth of field and focusing that occur when using standard imaging methods (Graham and Nimmo-Smith 2010).

The raw hologram, $I(x, y)$, is an intensity image recorded by a CCD containing constructive and destructive interference between the beam created from scattering by particles (E_0) within a sample volume and the incident collimated laser light (E_r). Terms E_0 and E_r are complex functions that describe the amplitude and phase of the respective light fields. In the terminology of holography, the complex field, E_0, is called the object wave, and E_r is the reference wave. Term E_0 is the light field composed of the sum of all diffracted waves by all scatterers in the sample volume. The recorded intensity is described by

$$I(x, y) = |E_0(x, y, z)e^{(ikz)} + E_r e^{(ikz)}|^2, \qquad (1)$$

where x, y is a 2D position within the raw image; z is the distance to the CCD of the camera from the object; i is the imaginary unit (which carries the phase of the respective light fields); e is the base of the natural logarithm; and wavenumber $k = 2\pi/\lambda$, which is the number of times the light has the same phase per unit space, where λ is the wavelength of incident light. This says that the recorded intensity is the square of the absolute value of the total field ($E_0 + E_r$). This is because a CCD responds only to light intensity; hence, the phase information
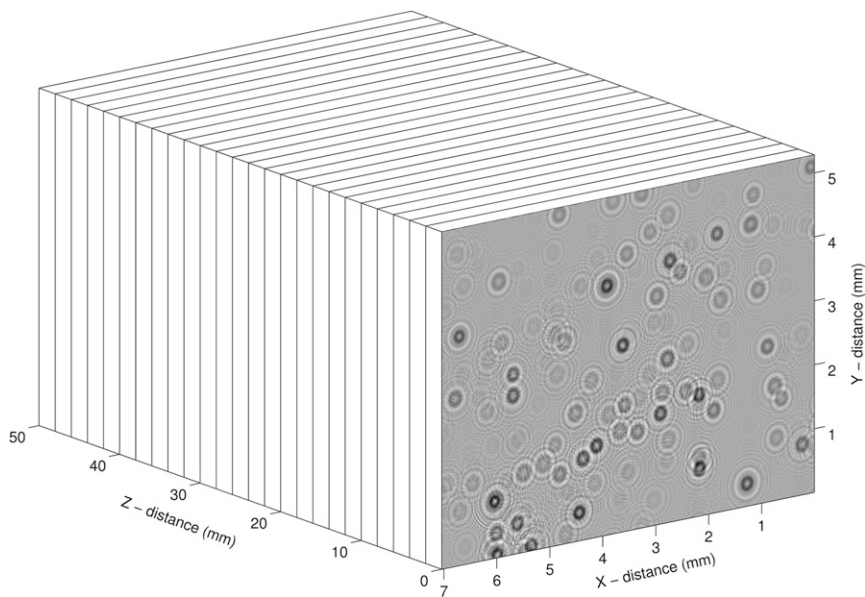
FIG. 1. Illustration of the holographic sample volume geometry and interference patterns.

of the complex (amplitude and phase) wave field is lost. The above-mentioned equation also implies that the recorded intensity is linearly proportional to the exposure, which is proportional to the intensity. Once $I(x, y)$ is obtained, the light field E_0 can be retrieved numerically using the principles of Fourier optics, as described in section 4a.

Three holographic camera configurations are used in this article to demonstrate the applicability of the numerical reconstruction method to multiple in-line holographic systems (Fig. 2). Each configuration (the specific mounting of the laser and CCD) is specifically adapted to suit a particular sampling strategy or marine environment. The system in Fig. 2a is capable of high-precision sample volume adjustments, and the sample volume can be narrowed to millimeter-scale widths for use in high concentrations (Graham and Nimmo-Smith 2010; Graham et al. 2012). The system shown in Fig. 2b also allows adjustable sample volume widths, but with a minimum width of about 1 cm, and is designed to minimize flow disruption around the sample volume during profiling (Graham et al. 2012; Cross et al. 2013, 2014). Finally, the system of Fig. 2c allows for the addition of alternative instrumentation for detailed comparisons of instrument responses (Davies et al. 2011). The laser beam is expanded before passing through the collimating optics. The collimation produces a beam that is most intense in the center, and the decay in laser intensity with distance from the center can be described by a two-dimensional Gaussian distribution. If the beam is collimated to a diameter much larger than the CCD

size, and so that the peak of the Gaussian intensity distribution is centered within the frame, this substantially reduces the change in intensity over the radial cross section of the image. This is implemented for the systems shown in Figs. 2a and 2b. For the system shown in Fig. 2c, however, the beam is collimated to a diameter that enables all the light to fall within the area of the CCD, so that the same cross section is also recorded by the LISST-100 component of the system.

3. Data

We draw upon data covering a range of particle types, shapes, and sizes, collected using a variety of holographic systems (in the laboratory and in situ). For verification that the automated holographic reconstruction can accurately resolve particle size distributions, sieved basalt spheres were recorded using the system described by Davies et al. (2011) and illustrated in Fig. 2c.

Field data were used for the automated classification of particles, collected within the surfzone of an energetic macrotidal sand beach (Praa Sands in southwest Cornwall, United Kingdom). The streamlined in-line system, as shown in Fig. 2b, with an 11-mm pathlength, has a very low profile that makes it suitable for deployment close to the bed. The system provided holographic images of near-bed suspended particles and bubbles in situ for the first time within the surfzone, during a total of 15 semidiurnal tidal cycles, at 5 Hz for 1-min "bursts" every 30 min during mid- to high tide (Conley et al. 2012). The
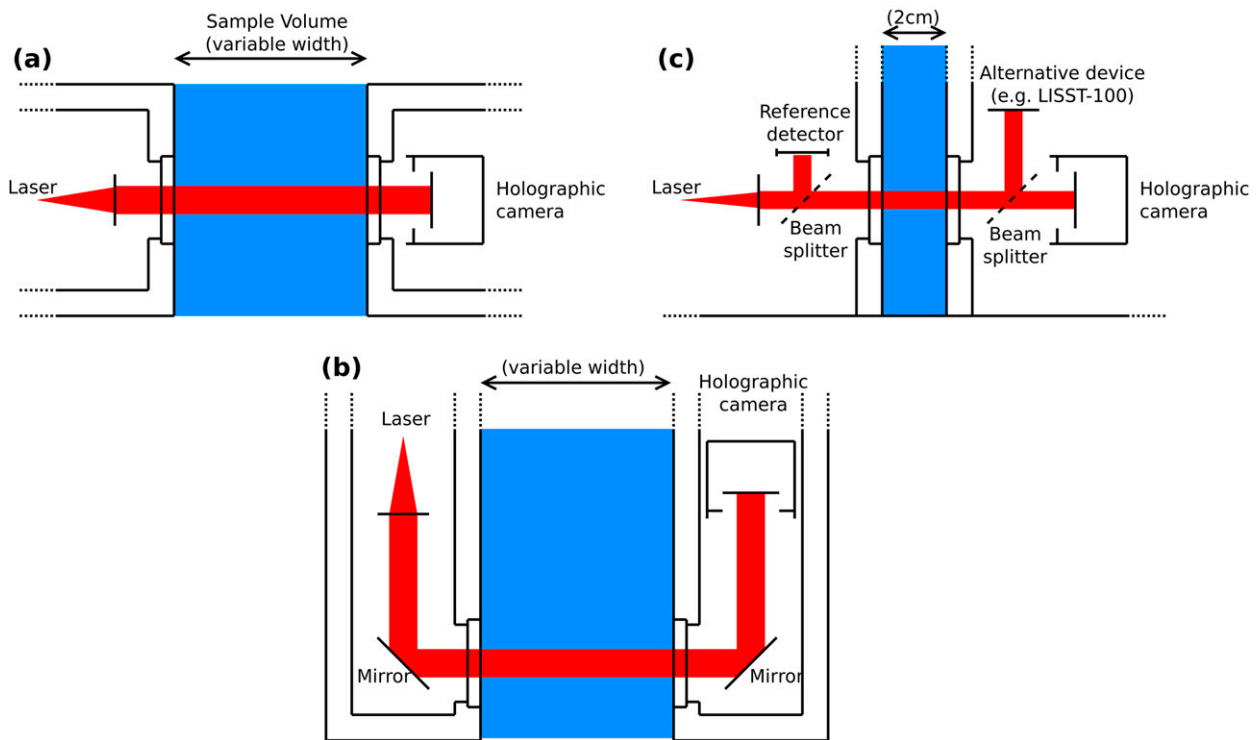
FIG. 2. Schematic illustrations of optical configurations of the holographic systems used in this study, with (a) nose-to-nose, (b) streamlined/profiling, and (c) combined systems. For each setup, a collimated laser beam passes through the sample volume and is recorded by the CCD of the camera, positioned on the far side of the volume. Scattering of light from within the beam interferes with the incident light of the initial beam, creating an interference pattern on the CCD camera.

dataset is composed of thousands of holograms from 17 bursts, encompassing the full spectrum of observed flow conditions in order to maximize the variation in relative abundances of sands, bubbles, and diatoms.

Montages of randomly selected particles from three 1-min bursts of field data (Fig. 3) illustrate the often surprising variability of suspended particle composition. Instantaneous concentrations of sand particles, bubbles, and phytoplankton were highly variable in time. Observed phytoplankton populations were overwhelmingly composed of diatom chains. Flocculated particles and zooplankton were absent in this very high-energy environment. A means by which particles can be classified by type was developed in order to avoid errors in calculated sand concentrations that would otherwise result from the variability in relative proportions of particle types. In this specific situation, it quickly becomes apparent that if all imaged particles were classified as sand when deriving concentrations, estimates of total suspended sand would have significant errors. These errors would not be systematic because the relative abundance of nonsand particles would depend on flow conditions.

Each hologram, representing a 1.7-mm^3 sample volume, was digitally reconstructed at 1-mm depth intervals.

Each particle in every reconstructed hologram was viewed on screen and classified by eye by a trained operative. The outlines of each particle were digitized by a trained operative who also classified each particle into either ''sand,'' ''bubble,'' or ''organic.'' Particles in a total of 5100 images were measured and classified in this way. A variety of metrics was generated from the digitized particle outlines. We felt confident in our ability to manually classify particles into these three visually distinct groupings, for example (with reference to Fig. 3), bubbles often contained concentric rings; sand grains were almost always convex and more angular than bubbles; diatom chains are nearly always long and thin, and often the individual cells were visible. Operator errors are somewhat inevitable considering factors such as partial reconstruction or blurring of some particles, very small particles (resolution issues), and the large number of particles measured (human fatigue). However, mindful of these sources of error, which are hard to reliably quantify, these manual measurements and classifications were nevertheless treated as the standard against which an automated classification technique could be developed and evaluated.
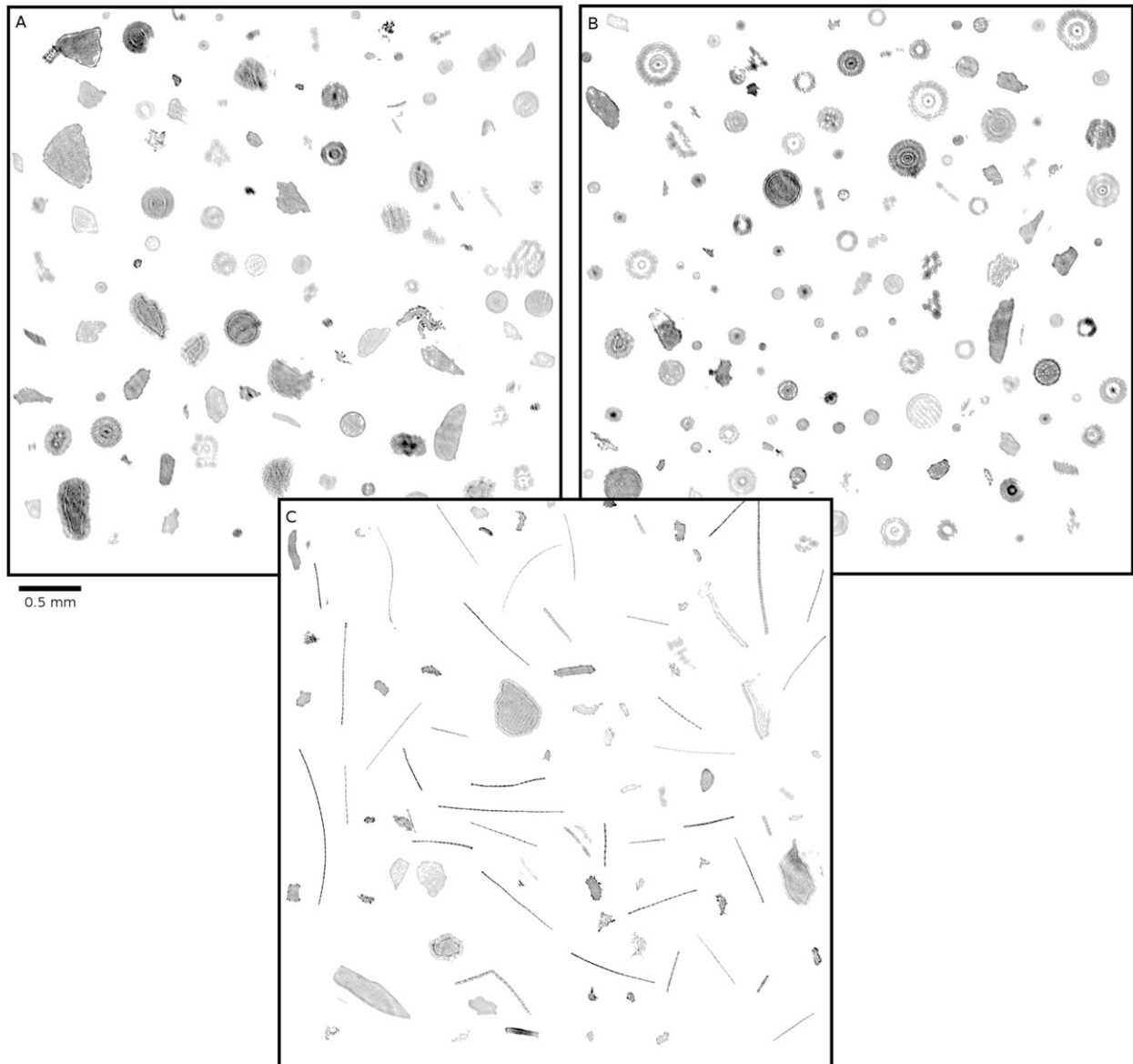
0.5 mm

FIG. 3. Montages of randomly selected and positioned particles within three 1-min bursts of field data collected in the surfzone 10 cm above the bed. Such montages provide a visual snapshot of the population of particles present. (top left) Burst A is characterized by sand particles and similar size bubbles, and is typical of the dataset as a whole. (top right) Burst B contains a relatively high concentration of bubbles. (bottom) Burst C contains an unusually high concentration of diatoms.

4. Methods

a. Holographic reconstruction and particle characterization

The workflow for automatic reconstruction of holograms, and the identification and sizing of particles therein, is detailed in this section. These holographic reconstruction routines have been improved from that of Graham and Nimmo-Smith (2010) and Owen and Zozulya (2000), and are available via a user community website (www.marinephysics.org/holoproc) and

have been incorporated into software shipped with the LISST-Holo.

The first processing stage is to correct for spatial variability in the background intensity of the raw images, which reduces noise and removes stationary objects that may be present on the optical components. This is achieved by subtracting the background image of the 2D intensity distribution from each raw hologram, either from clear water or an average of a number of images (Fig. 4). The number of images used to calculate a background from averaging is dependent on the variability and
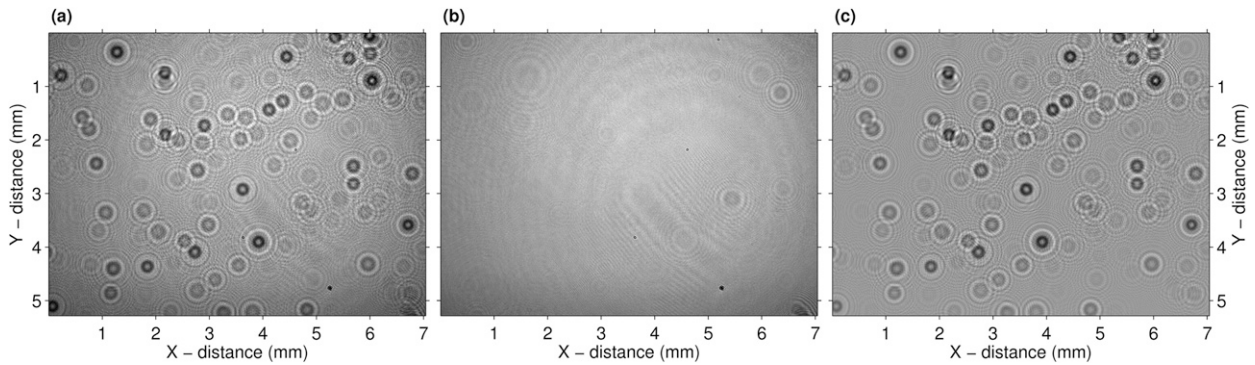
FIG. 4. Example of (a) a raw hologram containing particles, (b) background image, and (c) corrected image following background removal.

concentration of particles present in the images, typically of the order of 50 images or more. Averaging must be performed over a sufficiently large set of images so that the result is indistinguishable from that of a clean-water image (i.e., all movable objects are removed). Moving or binned averages may also be necessary in situations involving long time series where biofouling is significant, or where the instrument alignment changes slightly with water depth.

The background-corrected raw image is numerically reconstructed following Owen and Zozulya (2000), to produce an array of real-value images, focused at different positions (z) through the sample volume. Each particle within the reconstructed image stack is then focused and binarized, resulting in a single, concatenated binary image of all in-focus particles in the sample volume. Each particle in the binarized image is analyzed independently to return its geometrical properties, such as equivalent spherical diameter, perimeter, and major axis length (Graham and Nimmo-Smith 2010).

Owen and Zozulya (2000) demonstrate that the real image can be retrieved at any point within the sample by numerically propagating light back through the interference pattern, $I(x, y)$, using the routine summarized here.

Term $I(x, y)$ is transformed into the Fourier domain (f_1, f_2):

$$\hat{E}(f_1, f_2) = \frac{1}{(2\pi)^2} \iint dx\, dy\, I(x, y) e^{(if_1 x - if_2 y)}. \quad (2)$$

The part of the beam that is not diffracted (dc component) is then zeroed, and $\hat{E}(f_1, f_2)$ is shifted so that the dc component is in the center of the image. Term $\hat{E}$ is then multiplied by a phase factor that allows propagation back to a distance from the CCD corresponding to the location of the real image (z):

$$\hat{E}'(f_1, f_2, z) = \hat{E}(f_1, f_2) e^{\{-i[(\pi/P_s)|f_1 + f_2|]^2 z/2k\}}, \quad (3)$$

where P_s is the width of each CCD pixel.

The real-value image at distance z is obtained by applying the inverse Fourier transform of $\hat{E}'$:

$$E(x, y, z) = \left| \frac{1}{2\pi} \iint df_1\, df_2\, \hat{E}'(f_1, f_2, z) e^{(if_1 x + if_2 y)} \right|^2. \quad (4)$$

An improvement to the routine presented by Graham and Nimmo-Smith (2010) and Owen and Zozulya (2000) is an additional step to reduce noise created by the reconstruction, which hampers the success of the subsequent stages of binarization and particle identification. Areas between the particles within the reconstructed planes shown in Fig. 5 contain light gray pixels, which is an example of the type of noise that is problematic. To combat this, the lowest intensities of $E(x, y, z)$ are removed using a predetermined threshold (usually less than 2% of the maximum intensity of E). Noise removal substantially increases the accuracy of locating particles in the subsequent stages because particle edges become sharper. However, if the predetermined percentage for noise removal is too high (i.e., much greater than 2%), then the likelihood of large particle segmentation and loss of small particles will increase. Typically, a higher percentage can be applied in situations where the particles are more opaque, and subsequently stand out more from the background image noise. Populations of highly transparent particles, on the other hand, may become segmented more easily if this percentage exceeds about 0.5%. The reconstructed particles shown in Fig. 3 are much sharper than similar previously published images (e.g., Fig. 11 of Graham et al. 2012); this increase in quality results from the noise removal step.

Following Graham and Nimmo-Smith (2010), a binarization is performed on the histogram of standard deviations, $\sigma(x, y)$, through the stack of real images:

$$\sigma(x, y) = \left(\frac{1}{n-1} \right) \sum_{z=1} [E(x, y, z) - \overline{E}(x, y)]^2, \quad (5)$$
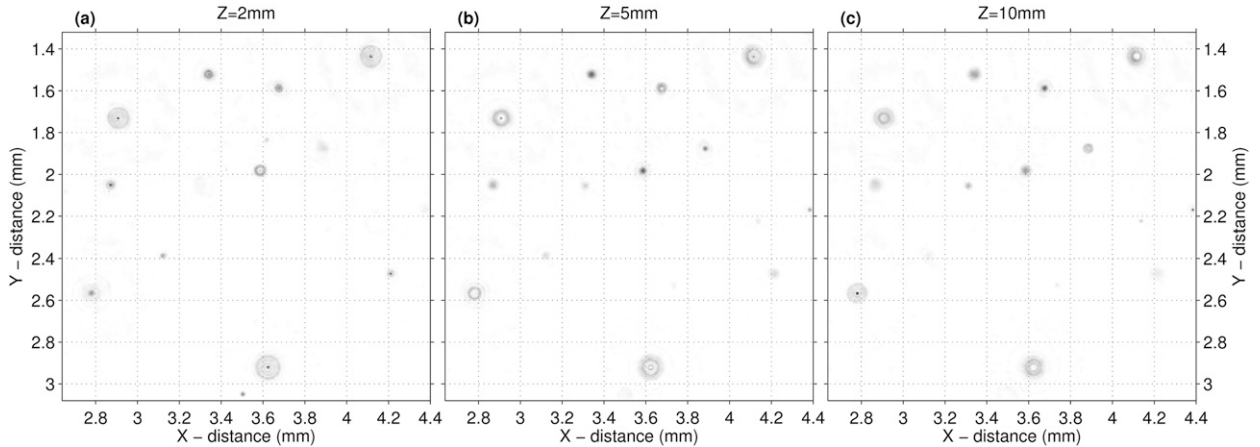
FIG. 5. Examples of segments of real images $[E(x, y)]$ from the reconstructed hologram of Fig. 4c at three depths through the sample volume.

where n is the number of real images that have been reconstructed at z distances, and $\overline{E}$ is the mean of $E(x, y, z)$ through all z planes:

$$\overline{E}(x, y) = \frac{1}{n} \sum_{z=1} E(x, y, z). \qquad (6)$$

Particles are located using an automatic global threshold based on the method of Otsu (1979), which minimizes the variance of pixel intensities between the foreground (particles) and background (water). A predetermined minimum threshold condition (usually within the range 0.05–0.2) is specified to reduce potential bias from unusually bright particles within a hologram. Increasing this minimum threshold can reduce small speckle noise, but it also has the potential to increase the chance of falsely segmenting large particles and/or missing small particles.

Each of the identified particles (p) at locations within pixel ranges specified by x_p (of length n_x pixels) and y_p (of length n_y pixels) may then be focused to a distance (z_F) at which the maximum total intensity of $E(x_p, y_p)$ is found in the stack of real images (Fig. 5):

$$z_F(p) = \arg\max_z \sum_{j=1}^{n_x} \sum_{k=1}^{n_y} E(x_{p(j)}, y_{p(k)}, z). \qquad (7)$$

The accuracy of this focusing is improved by the noise removal applied after Eq. (4) because the summing of $E(x_p, y_p, z)$ is not contaminated by background noise. A binary image of each particle, $E_B(x_p, y_p)$, is then created using a second, local binarization process that is performed on the focused segment of the real image, $E[x_p, y_p, z_F(p)]$, again using the method of Otsu (1979) but without a fixed minimum threshold. The fixed threshold is not required at this stage, as only one object

is expected within the region of interest, which creates a more prominent bimodal histogram of pixel intensities that is better suited to the Otsu method.

The method of binarizing $E[x_p, y_p, z_F(p)]$ into $E_B(x_p, y_p)$ often results in particles that contain false holes, especially in situations where the incident illumination is nonuniform or the intraparticle texture is highly variable. To reduce the potential for holes within the encompassing perimeter of each identified particle, a flood–fill operation is performed on each $E_B(x_p, y_p)$ image. Following this, a montage of all E_B images is created, each positioned within the original x, y coordinates of the raw image.

Particle areas are calculated from $E_B(x_p, y_p)$ images using pixel counting. The equivalent circular diameter (ECD) is used to represent particle size because it can be calculated from pixel areas, and also for the purposes of use in optical and acoustic scattering theories, which often assume spherical particles (e.g., Mie theory).

For a perfect analog in-line hologram (i.e., no pixel size artifacts), the smallest resolvable spherical particle (of diameter d_s) is governed entirely by the distance to the particle from the CCD (z) and the wavelength of incident light (λ). Vikram (1992) shows that this can be calculated as follows:

$$d_s = \sqrt{\frac{z\lambda}{100}}. \qquad (8)$$

Malkiel et al. (1999) demonstrate that this theoretical determination of d_s compares well to the minimum sizes resolved, and that nonspherical particles can be resolved at smaller sizes. However, given the highly variable shape of naturally occurring marine particles, and potential pixelation effects in digital holograms, we impose a conservative minimum limit ($A_{\min}$) to the area of
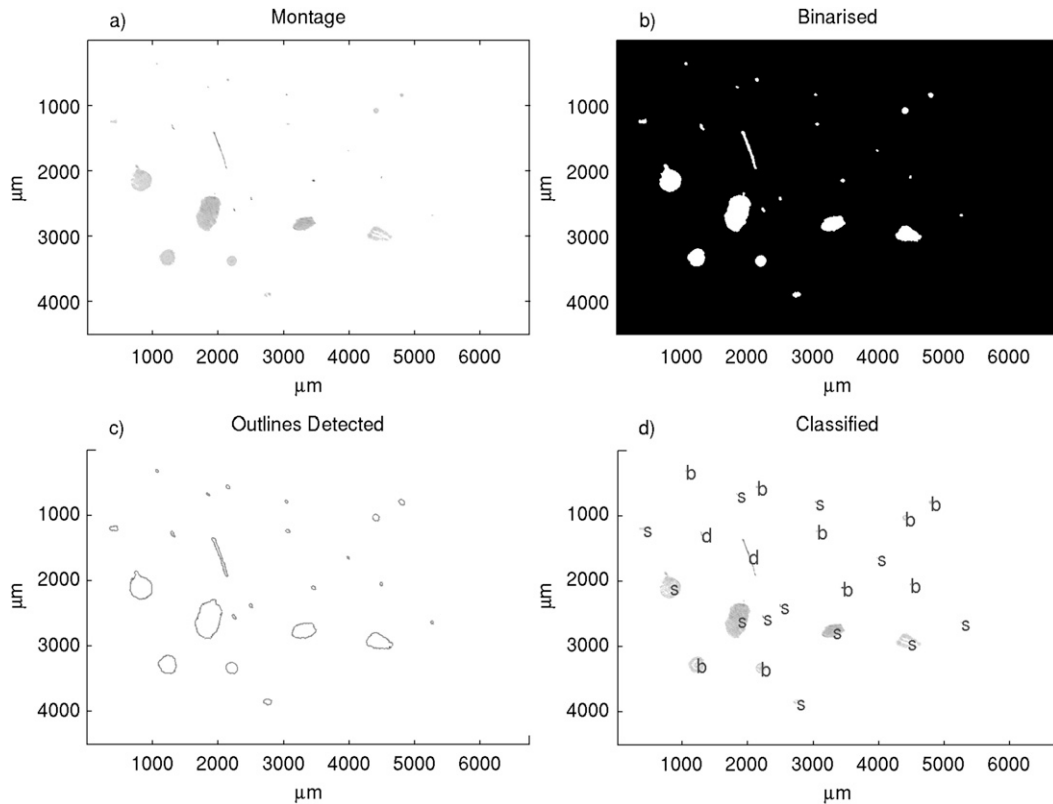
FIG. 6. Example stages from the workflow of the automated particle classification routine: (a) input montage of reconstructed particles from a single holographic image, (b) binarized image, (c) binarized image with the particle outlines detected, and (d) particles from the montage segmented and classified (''s'' is sand, ''b'' is bubble, and ''d'' is diatom).

pixels (of width P_s) that make up each particle returned by the binarization:

$$A_{\min} = \left\lceil \frac{1}{P_s^2} \pi \left(\frac{d_s}{2}\right)^2 \right\rceil. \tag{9}$$

Particles below this limit are ignored. The minimum pixel area is applied to the farthest distance possible in the sample volume and is rounded upward based on the size of the CCD pixels (P_s). For example, with the standard pathlength of the LISST-Holo ($z = 50$ mm; $\lambda = 658$ nm; $P_s = 4.4\,\mu$m), $A_{\min}$ is 14 square pixels.

In addition to discarding particles with areas below $A_{\min}$, any object that contains pixels within 64 pixels of the image border after binarization is also discarded. While it is possible to reconstruct an object using only a small portion of its interference pattern, the detail of the smaller scales of particle geometry are lost. The use of the 64-pixel-border clearing is to ensure that a sufficient portion of the holographic interference is captured from each particle in order to avoid errors in size estimates that result from only a portion of the particle falling within the field of view.

b. Particle classification

There are four steps to the automated classification and measurement procedure, which are applied to the final stages of the standard analysis routine described above. The first stage is to perform an additional hole-filling operation on the binary image (E_B) (Fig. 6b).

The second stage is to link up long, thin objects (such as diatom chains) that have only been partially reconstructed. To do this the image is morphologically dilated with a linear structural element of length two pixels and rotated from 0° to 275° orientations in increments of 22.5°. This has the effect of linking long, thin objects of arbitrary rotation. Once dilated, the reverse operation (erosion) is applied using the same structural element and the same rotations, which preserves the size of all objects in the image.

The third stage uses an alpha shape, computed using the Delaunay triangulation method of Edelsbrunner and Mücke (1994), to digitize the area and perimeter of each particle (Fig. 6c). Whereas the convex hull of an object is the smallest convex shape that can contain the

object, the alpha shape is the bounding contour of an object, so it can be convex or not, and therefore represents the shape of nonconvex objects more accurately than a convex hull. The circularity C of both the alpha shape and convex hull are then computed for each particle:

$$C = \frac{4\pi A}{P_r^2}, \tag{10}$$

where A and P_r are area and perimeter, respectively. A perfect circle has a circularity of 1 and a line is 0. We denote the circularity of the alpha shape and convex hull as C_a and C_h, respectively, and the area of the alpha shape and convex hull as A_a and A_h, respectively.

The final stage is the classification, which is carried out using the above-mentioned metrics. An object is classified as a bubble if $C_a > 0.85$ and $C_h > 0.85$. If an object is really a bubble, it will be very circular (but not necessarily perfectly circular), and its alpha shape as well as its convex hull will be very similar. An object is classified as a diatom if $C_a < 0.5$ and $A_h/A_a < 0.9$. A diatom is not very circular, and the difference between its alpha shape and its convex hull will be large. All other objects are classified as sand grains (Fig. 6d).

5. Results

a. Particle size

Figure 7 summarizes some example images of basalt spherical standards, and their associated size distributions, which were analyzed automatically (red) and manually (green) using the system shown in Fig. 2c. Vertical black lines indicate the limits of the sieved ranges of each sample for the following sizes: $90 - 106 \, \mu m$ (Figs. 7a–c), $125 - 150 \, \mu m$ (Figs. 7d–f), $180 - 212 \, \mu m$ (Figs. 7g–i), and $250 - 300 \, \mu m$ (Figs. 7j–l).

Automated and manual analyses return volume distributions with modes within the limits of the sieved ranges. The images of raw holograms superimposed with the binarized particles (Figs. 7a and 7b) show that there are a number of particles that are missed by both methods, resulting in an underestimate of concentration. This problem is emphasized by the weaker intensities toward the edges of the beam, where particles do not accurately binarize and are subsequently more easily discarded by both the automated and manual methods. The edge-of-beam issues are less problematic for standard systems such as those shown in Figs. 2a and 2b, where the beam diameter is much larger than the CCD size. Despite the configuration-specific concentration errors, the size estimates agree well between the manual and automated analyses, but with some additional small particles returned by the automated processing.

A similar analysis of the same sample of sieved basalt spheres was conducted by Davies et al. (2011) to compare the responses of holography with the laser diffraction (e.g., LISST-100x). Graham and Nimmo-Smith (2010) also validated the holographic system shown in Fig. 2a against a Malvern laser diffractometer. Both of these studies showed that laser diffraction and holography report very similar volume distributions for simplistic particle shapes.

The data presented in Fig. 8 were obtained from the combined holographic camera and LISST-100 system, described by Davies et al. (2011). For this system, segmentation occurs near the edges of the beam, where the intensity of incident light is lower. The large particle in Fig. 8a is broken up in the following frame (Fig. 8b) as it moves out of the bright, middle part of the beam. The effect of segmentation on the resulting volume distribution is illustrated in Fig. 8c, with the solid line representing the equivalent circular diameter from Fig. 8a, and the dashed line representing the distribution obtained from Fig. 8b. The size distribution from frames where there is no segmentation shows a strong peak in volume concentration in the 331-μm size class and a low concentration of small particles $(50 - 100 \, \mu m)$. The distribution from Fig. 8b, where the largest particle has become segmented, shows a reduction in particle size of the large particle by about $100 \, \mu m$ (right-hand peak in Fig. 8c). The segmented distribution shows an increase in the volume concentration of smaller particles between diameters of 50 and $100 \, \mu m$, which is the result of smaller segments from the large particle. These changes in volume distributions do not conserve the total volume concentration in comparison to the nonsegmented equivalent, because some area of the segmented particle is lost through the introduction of gaps and holes. In this illustration, a reduction in total volume concentration by 57% is observed between Figs. 8a and 8b. In a typical in situ sampling situation, however, the reduction in total concentration and shift in size distribution is likely to be much less substantial because a much lower percentage of the particles in the frame will be subjected to such a harsh segmentation than that which is illustrated in Fig. 8.

b. Particle classification

The ability to classify particles makes a substantial difference to the accuracy of particle concentration measurements. Volumetric concentrations were estimated for each image in the field data described in section 3: 1) including just sand particles, and 2) including bubbles and organic particles as well. The mean volumetric difference over a burst of images varies between 15% and 84%, with a typical per-burst difference
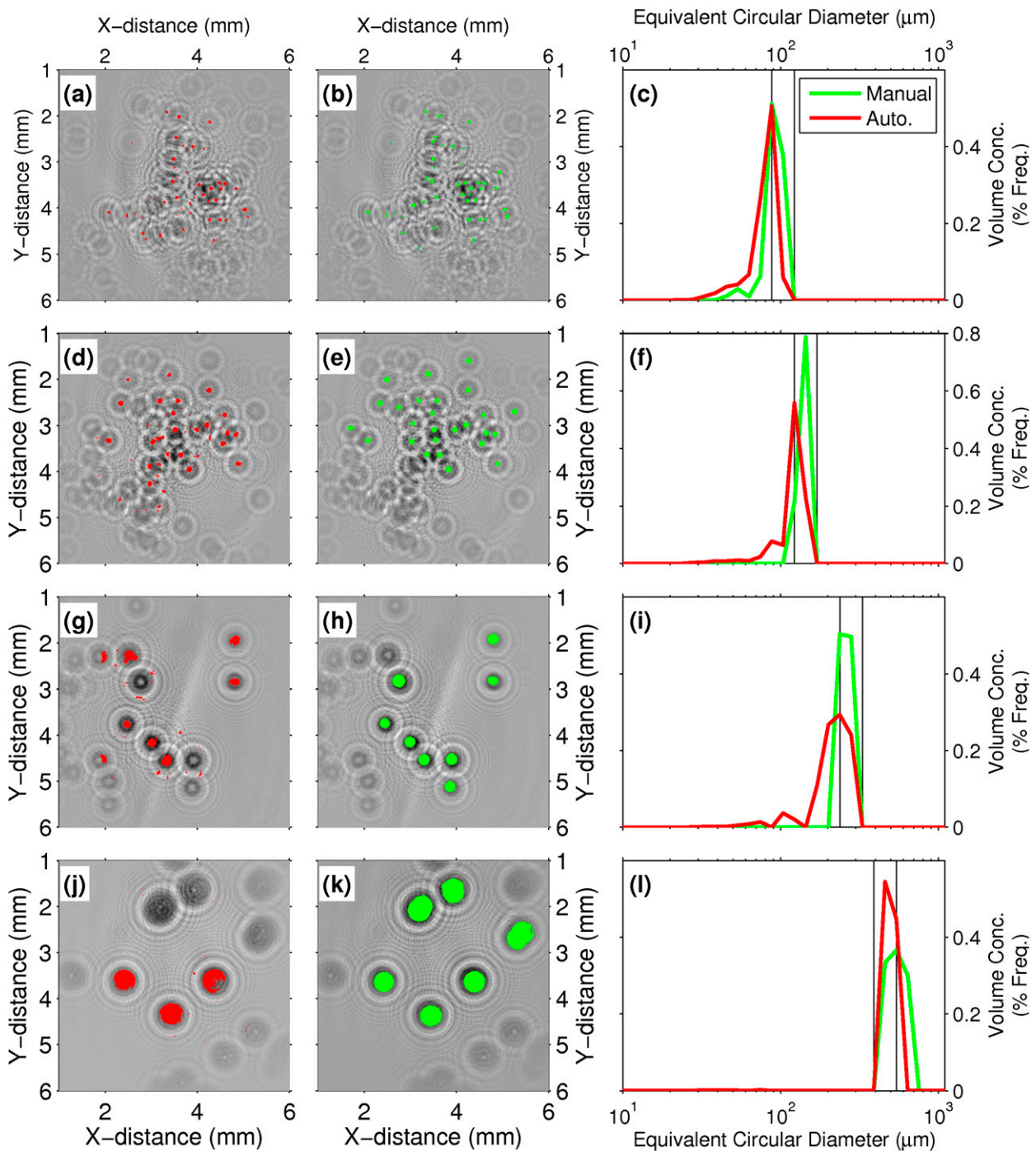
FIG. 7. Examples of volume distributions for sieved Basalt spheres that were analyzed automatically (red) and manually (green). Vertical black lines indicate the limits of the sieved ranges of each sample for the following sizes: (a)–(c) 90–106 μm, (d)–(f) 125–150 μm, (g)–(i) 180–212 μm, and (j)–(l) 250–300 μm.

of 46%. Given the relative densities of bubbles, sand, and diatoms, the relative difference in mass concentrations would be even higher.

The shape parameters used for automated particle classification are shown in Fig. 9. The automatic separation

of diatoms ($C_a < 0.5$ and $A_h/A_a < 0.9$), bubbles ($C_a > 0.85$ and $C_h > 0.85$), and sand (via elimination of diatoms and bubbles) is compared with associated manual identification, as indicated by the data-point shade. This style of data visualization is a simple, effective means by which to
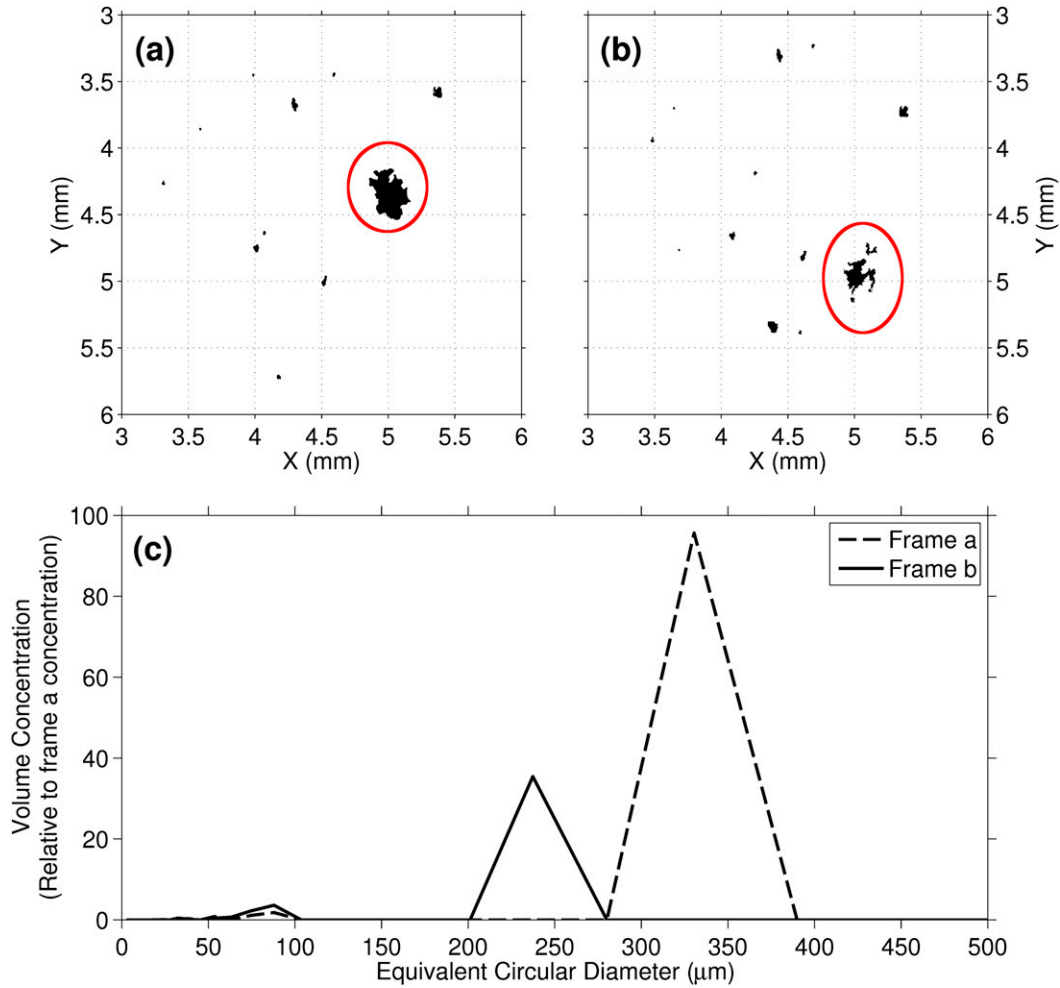
FIG. 8. (a) Example region of a binary image showing a large, intact particle. (b) A large particle has settled into an area of lower incident light intensity. (c) The ECD distributions from (a) and (b), with the dashed line representing the distribution from (a) and the solid line representing the distribution from (b).

qualitatively assess the skill of the classification method and for setting thresholds for the shape parameters used to discriminate between particle types, for use with other datasets from different environments.

The probability that the automated technique correctly classified a given particle is always over 0.6. Evaluating this skill requires calculating the probability that a given set of classifications on all particles, in a given image within this tripartite classification scheme, would arise by chance. This is conditional on the relative abundances of each particle type and, given it is a probability without replacement, also the sequence in which the particles are classified. This probability is given by

$$P = \frac{(!N_{\text{sand}} + !N_{\text{bubbles}} + !N_{\text{diatoms}})}{(!N_{\text{total}})}, \quad (11)$$

where N denotes absolute number and N_{total} is the total number of particles present. Therefore, no simple relationship exists between P and N_{total} because it depends on the specific population of particles present, and $P/(!N_{\text{total}})$ is an exponential function of N_{total}, meaning that if the relative proportions stayed the same but the total number of particles increased, then the odds of a given classification by chance would lessen exponentially. The classification probability is always at least an order of magnitude greater than by chance. Therefore, the automated routine performed well, especially given the number of individual grains present in each image ranged from $O(1)$ to $O(10)$.

Particle areas per particle type were summed for each sample (collected at a frequency of 5 Hz), and averaged over 1 s. There is both bias and scatter present in comparisons, aggregated over all 17 bursts, between manual
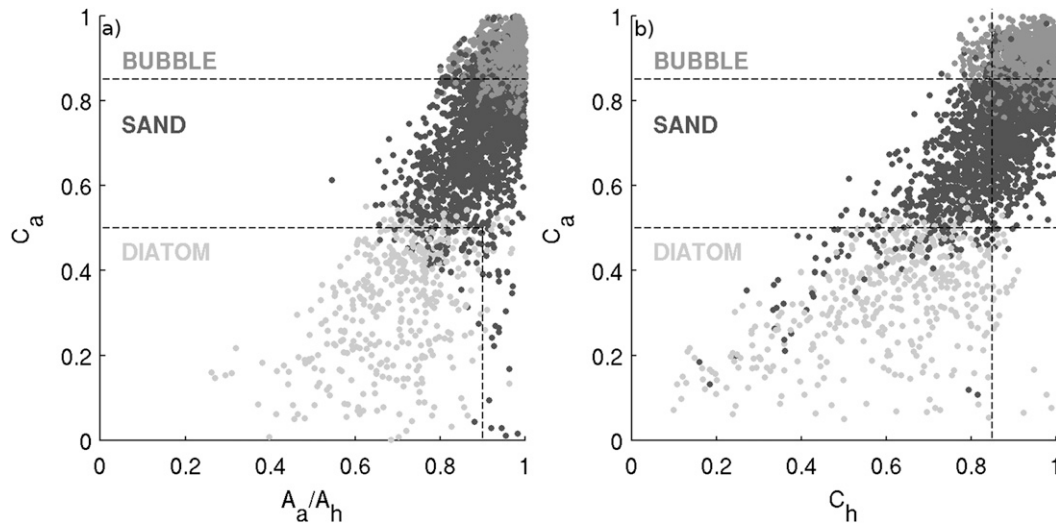
FIG. 9. Automated parameters used for (a) diatom and (b) bubble classification of particles measured during bursts A–C (Fig. 3), with data points colored according to manual classifications.

and automated metrics of total particle area for mineral sands, bubbles, and diatoms (Figs. 10d–f). All estimates fall within 100% of the true value for sand grains and bubbles. For diatoms, around 60% of estimates fall within 100% of the true value.

A similar analysis was conducted for mean (over a sample) equivalent circular diameters (Figs. 10a–c). All estimates fall within 100% of the true value for sand grains and bubbles. For diatoms, around 90% of the estimates fall within 100% of the true value. Estimates of sand grain mean diameters are more homoscedastic, with regression intercepts close to zero and slopes close to 1. In contrast, estimates of bubble diameters show very little scatter, but the regression slopes are large with systematic underestimation below a certain size. Estimates of diatom diameters are surprisingly good considering the relative failings of the method for diatom area estimates.

6. Discussion

Results from both estimations of particle size distributions and automatic particle classification show that holographic particle imaging provides an accurate and flexible technique for a wide range of purposes. Below, the results from automated sizing and classification are discussed separately.

a. Particle size

Additional small particles may be counted into the resultant particle size distributions (PSD; Fig. 7), either due to incorrect binarization of noise or from artificial segmentation of larger particles into multiple smaller particles, caused by a threshold that is too high. The relatively small particles that have been incorrectly binarized (e.g., Figure 7g) have no identifiable interference patterns surrounding them. Caution should therefore be applied to the interpretation of the smallest particles returned by the automated routine. However, the effect of the smallest particles on the calculated volume distributions will be minimal if appropriate thresholds and noise removal are applied.

Segmentation errors usually occur when a large particle has a low signal response in the focused reconstructed slice $E(x_p, y_p)$. This causes the area covered by a particle to become harder to isolate from the background noise in the image, making a single threshold for binarization difficult to determine. With a threshold too low, the binary particle will become dilated, resulting in area overestimates. A threshold too high results in holes appearing in the particle and segments of the particle breaking up, leading to an underestimate of the particle area and an increase in the apparent number of smaller particles from the detached segments.

While it is possible to process images using settings conducive to either systematically over- or undersegmenting particles (producing a large bias in derived particle statistics), it is likely that both under- and oversegmenting occurs simultaneously within in situ datasets. This tends to minimize bias in derived particle sizes but can induce a significant degree of scatter. The scatter depends specifically on the particle population and the specific parameters used in processing. Unfortunately, it is hard to quantify the effect of segmentation for in situ datasets because large particles are rarely, if ever, present in consecutive frames due to the
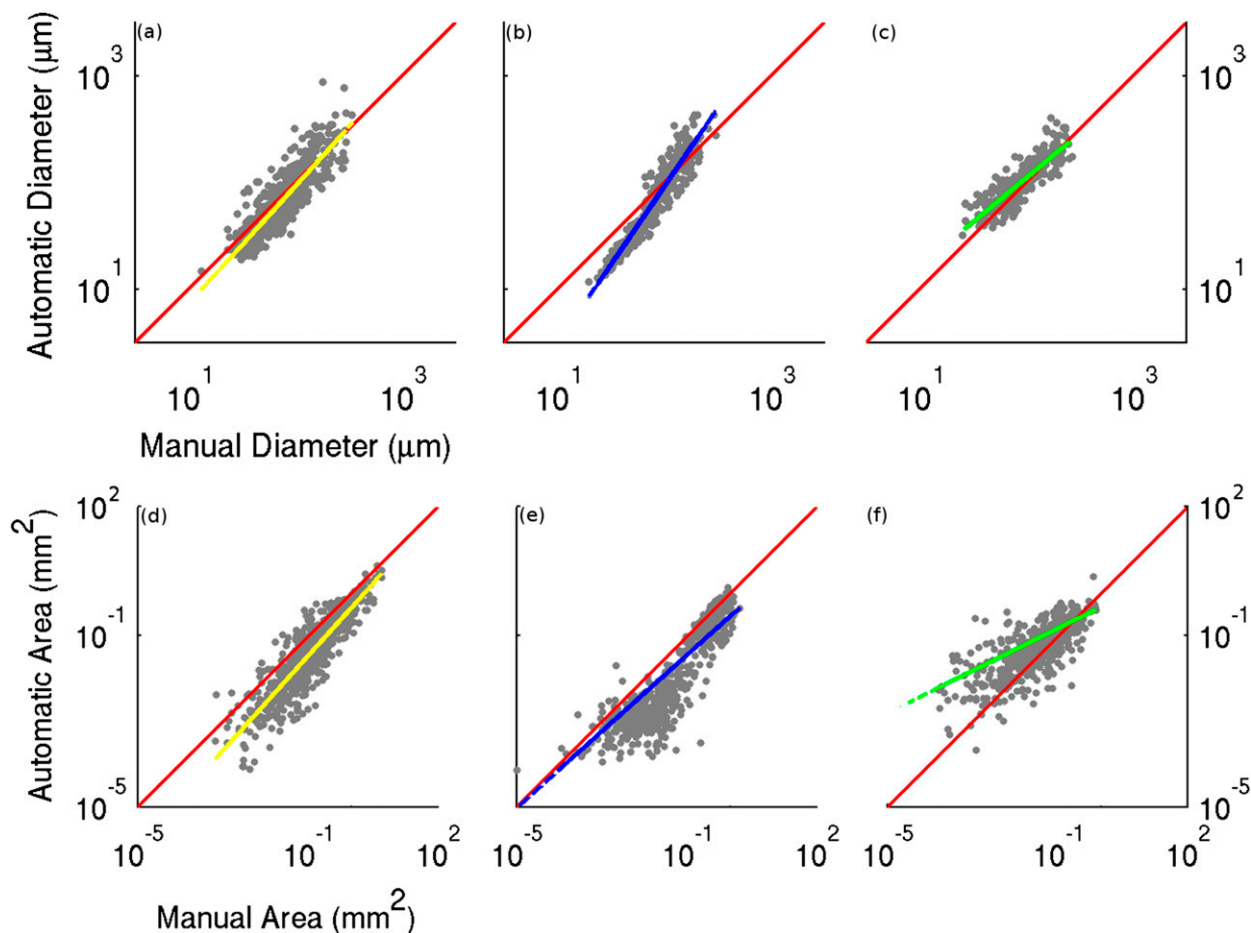
FIG. 10. Manual vs automated (a)–(c) total particle ECD and (d)–(f) area for (a),(d) sand, (b),(e) bubbles, and (c),(f) and diatoms using 1-s averages. Solid red line is the 1:1 relationship, and lighter colored line is the linear least squares fit.

higher flow speeds (if the instrument is in a fixed location) or due to instrument movement (e.g., during profiling). In short, particle size distributions containing oversegmented particles, such as that illustrated in Fig. 8, results from poor incident illumination and will cause overestimates of small particles and underestimates of total volume concentration.

b. Particle classification

Much previous work on particle holography has focused on one type of particle or organism (e.g., Malkiel et al. 2004, 2006; Sheng et al. 2006, 2007; Katz and Sheng 2010). Where it is important to distinguish between particle types, automated classification of particles in holographic imagery offers unique challenges. Particles often have irregular, fuzzy, or incomplete outlines, and are oriented freely within the sample volume. Focused silhouettes of bubbles, which are spherical or near spherical, will often have nonsmooth outlines. Particles may even be broken up, for example, long diatom chains, which

may only be partially present across multiple planes. The image may be oversegmented, which causes a decrease in the number of large particles and an increase in small particles from artificially broken segments of a particle, or the image may be undersegmented if adjacent grains (possibly overlapping) are not separated. Here, we have outlined a simple approach to the specific problem of differentiating between sand, diatoms, and bubbles, but similar principles could be applied to a wide variety of mixed particle populations. For these reasons, previous studies have relied on manual (visual) discrimination between mixed particle types in holographic image reconstructions (Conley et al. 2012; Cross et al. 2013).

There are a number of particle metrics with which one could evaluate the performance of an automated particle classification routine. Particle area and equivalent circular diameter were chosen because of their relevance to the intended research use of the data from the automated routine, which was to evaluate the performance

of an acoustic backscatter sensor (predominantly sensitive to the particle cross-sectional area) and is the subject of a forthcoming paper. We argue that choosing other metrics would be equally valid and the difference in interpretation of the skill of the method largely qualitative.

Incorrect classifications within this tripartite classification scheme were found to be a random source of error that tends to average out over one sample (all particles in one montage image) and further over several consecutive samples. We decided that further comparisons would not be made on a particle-by-particle basis, but rather on a sample basis. Given the nature of data classified into discrete groups, summing or averaging on a frame-by-frame basis makes the within-sample variances negligible and the between-sample variances a more true reflection of the error of the method compared to an independent measurement technique.

We suggest that the automated routine will be more prone to misclassification errors than measurement errors that are caused by over- or undersegmentation. The errors caused by measurement tend to be random (i.e., oversegmentation is approximately as likely as undersegmentation). In contrast, errors caused by misclassification are more likely to be systematic, causing a slope in the regression line that departs from the 1:1 relationship. The scatter systematically reduces with averaging period, indicative that the scatter is caused by measurement errors. Sand and bubble areas tend to be slightly underestimated by the automated routine, with no strong tendency for this bias as a function of concentration. In contrast, diatom areas tend to be overestimated, and this overestimation is worsened in lower concentrations. Systematic errors in one particle type cause errors in the other two. In general, too many small bubbles and sand grains are being misclassified as diatoms. The source of these errors is related to one set of shape thresholds being used for all 17 bursts, in which the reconstruction quality differed. It is unlikely that sand grains and bubbles varied significantly in shape; however, diatoms did vary in shape significantly, so it is more difficult to automatically classify those particles based on shape alone.

The simple rule-based approach to classification based on object shape has the advantage that it is easy to understand and implement, and in this case it reduces the uncertainty in particle identification to an acceptable level by improving estimates of sand transport. The method suffers the disadvantage that in order to be transferable to other populations of particles (such as other phytoplankton, zooplankton, and mineral particles with shapes significantly different from sand grains), the rules and thresholds may have to be modified. All

thresholds in the above-mentioned classification were derived empirically from the set of manual observations and are therefore likely to change if applied to a different dataset. Performance could have been improved if thresholds were adjusted to optimum levels per burst, however, that partly defeats the purpose of an automated routine. Classifying particles based on shape is found to be sufficient for the three particle types of interest here. However, for differentiating more complex shapes (such as plankton and cohesive sediments), textural information might also be required for satisfactory results. Improved, more objective, automated particle classifications could be achieved by adapting pattern recognition and machine-learning algorithms designed for conventional photographic imagery (e.g., Culverhouse et al. 1996; Davis et al. 2004; Benfield et al. 2007; Gorsky et al. 2010; MacLeod et al. 2010) to holographic imagery.

7. Conclusions

The use of automatic holographic image processing enables rapid and accurate analysis of large datasets. The holographic image processing improvements detailed here have substantially enhanced the quality of reconstructed particle images and have enabled accurate particle size distributions to be calculated without the need for excessive manual supervision. We have compared manual and automated particle size distributions, which were in good agreement over diameters from 90 to 500 μm. In addition, we have validated particle classifications against manual equivalents, which were also in generally good agreement, indicating that the automatic holographic reconstruction routines used were reliable for many applications of marine particle analysis.

The accurate characterization of particle shape by way of automatic holographic image processing has allowed for an autonomous shape-based particle classification to be developed. To test this classification system, holographic images of suspended sand, diatoms, and entrained bubbles were obtained near the bed in an energetic surfzone. The skill of the technique in correctly classifying a given particle, in a tripartite classification compared to the manual classification of that particle, is greater than 60% and is always greater than a correct classification by chance. Root-mean-square errors decreased upon averaging over successively larger time scales, in a manner consistent with the nonsystematic nature of measurement errors. In contrast, biases were observed between automated and manual estimates due to some systematic misclassification of diatoms. We suggest that this is due to the larger

variability in phytoplankton shapes than that which is accounted for by the simple classification.

Future particle classification methods may benefit from a combination of shape and particle surface texture, which could be obtained from reconstructed holograms. We also recommend that future developments of holographic reconstruction routines should be primarily targeted at reducing oversegmentation of large particles and utilizing methods to separate overlapping particles.

REFERENCES

Agrawal, Y. C., A. Whitmire, O. A. Mikkelsen, and H. C. Pottsmith, 2008: Light scattering by random shaped particles and consequences on measuring suspended sediments by laser diffraction. *J. Geophys. Res.,* **113,** C04023, doi:10.1029/2007JC004403.

Andrews, S., D. Nover, and S. G. Schladow, 2010: Using laser diffraction data to obtain accurate particle size distributions: The role of particle composition. *Limnol. Oceanogr. Methods,* **8,** 507–526, doi:10.4319/lom.2010.8.507.

Benfield, M., and Coauthors, 2007: RAPID: Research on Automated Plankton Identification. *Oceanography,* **20,** 172–187, doi:10.5670/oceanog.2007.63.

Conley, D. C., D. Buscombe, and W. A. M. Nimmo-Smith, 2012: Use of digital holographic cameras to examine the measurement and understanding of sediment suspension in the nearshore. *Proceedings of the 33rd Conference on Coastal Engineering,* P. Lynett and J. McKee Smith, Eds., Vol. 2, ICCE, 990–1000.

Cross, J., W. A. M. Nimmo-Smith, R. Torres, and P. J. Hosegood, 2013: Biological controls on resuspension and the relationship between particle size and the Kolmogorov length scale in a shallow coastal sea. *Mar. Geol.,* **343,** 29–38, doi:10.1016/j.margeo.2013.06.014.

——, ——, P. J. Hosegood, and R. Torres, 2014: The dispersal of phytoplankton populations by enhanced turbulent mixing in a shallow coastal sea. *J. Mar. Syst.,* **136,** 55–64, doi:10.1016/j.jmarsys.2014.03.009.

Culverhouse, P., and Coauthors, 1996: Automatic classification of field-collected dinoflagellates by artificial neural network. *Mar. Ecol. Prog. Ser.,* **139,** 281–287, doi:10.3354/meps139281.

Davies, E. J., W. A. M. Nimmo-Smith, Y. C. Agrawal, and A. J. Souza, 2011: Scattering signatures of suspended particles: An integrated system for combining digital holography and laser diffraction. *Opt. Express,* **19,** 25 488–25 499, doi:10.1364/OE.19.025488.

——, D. McKee, D. Bowers, G. W. Graham, and W. A. M. Nimmo-Smith, 2014: Optically significant particle sizes in seawater. *Appl. Opt.,* **53,** 1067–1074, doi:10.1364/AO.53.001067.

Davis, C., Q. Hu, S. Gallager, X. Tang, and C. Ashjian, 2004: Real-time observation of taxa-specific plankton distributions: An optical sampling method. *Mar. Ecol. Prog. Ser.,* **284,** 77–96, doi:10.3354/meps284077.

Edelsbrunner, H., and E. P. Mücke, 1994: Three-dimensional alpha shapes. *ACM Trans. Graphics,* **13,** 43–72, doi:10.1145/174462.156635.

Gorsky, G., and Coauthors, 2010: Digital zooplankton image analysis using the ZooScan integrated system. *J. Plankton Res.,* **32,** 285–303, doi:10.1093/plankt/fbp124.

Graham, G. W., and W. A. M. Nimmo-Smith, 2010: The application of holography to the analysis of size and settling velocity of suspended cohesive sediments. *Limnol. Oceanogr. Methods,* **8,** 1–15, doi:10.4319/lom.2010.8.1.

——, E. J. Davies, W. A. M. Nimmo-Smith, D. G. Bowers, and K. M. Braithwaite, 2012: Interpreting LISST-100X measurements of particles with complex shape using digital in-line holography. *J. Geophys. Res.,* **117,** C05034, doi:10.1029/2011JC007613.

Katz, J., and J. Sheng, 2010: Applications of holography in fluid mechanics and particle dynamics. *Annu. Rev. Fluid Mech.,* **42,** 531–555, doi:10.1146/annurev-fluid-121108-145508.

MacLeod, N., M. Benfield, and P. Culverhouse, 2010: Time to automate identification. *Nature,* **467,** 154–155, doi:10.1038/467154a.

Malkiel, E., O. Alquaddoomi, and J. Katz, 1999: Measurements of plankton distribution in the ocean using submersible holography. *Meas. Sci. Technol.,* **10,** 1142, doi:10.1088/0957-0233/10/12/305.

——, J. Abras, and J. Katz, 2004: Automated scanning and measurements of particle distributions within a holographic reconstructed volume. *Meas. Sci. Technol.,* **15,** 601–612, doi:10.1088/0957-0233/15/4/001.

——, ——, E. Widder, and J. Katz, 2006: On the spatial distribution and nearest neighbor distance between particles in the water column determined from *in situ* holographic measurements. *J. Plankton Res.,* **28,** 149–170, doi:10.1093/plankt/fbi107.

Moate, B. D., and P. D. Thorne, 2012: Interpreting acoustic backscatter from suspended sediments of different and mixed mineralogical composition. *Cont. Shelf Res.,* **46,** 67–82, doi:10.1016/j.csr.2011.10.007.

Otsu, N., 1979: A threshold selection method from gray-level histogram. *IEEE Trans. Syst. Man Cybern.,* **9,** 62–66, doi:10.1109/TSMC.1979.4310076.

Owen, R. B., and A. A. Zozulya, 2000: In-line digital holographic sensor for monitoring and characterizing marine particulates. *Opt. Eng.,* **39,** 2187–2197, doi:10.1117/1.1305542.

Sheng, J., E. Malkiel, and J. Katz, 2006: Digital holographic microscope for measuring three-dimensional particle distributions and motions. *Appl. Opt.,* **45,** 3893–3901, doi:10.1364/AO.45.003893.

——, ——, ——, J. Adolf, R. Belas, and A. Place, 2007: Digital holographic microscopy reveals prey-induced changes in swimming behavior of predatory dinoflagellates. *Proc. Natl. Acad. Sci. USA,* **104,** 17 512–17 517, doi:10.1073/pnas.0704658104.

Stemmann, L., and E. Boss, 2012: Plankton and particle size and packaging: From determining optical properties to driving the biological pump. *Annu. Rev. Mar. Sci.,* **4,** 263–290, doi:10.1146/annurev-marine-120710-100853.

Sun, H., P. Benzie, N. Burns, D. Hendry, M. Player, and J. Watson, 2008: Underwater digital holography for studies of marine plankton. *Philos. Trans. Roy. Soc. London,* **366,** 1789–1806, doi:10.1098/rsta.2007.2187.

Thorne, P. D., and D. M. Hanes, 2002: A review of acoustic measurements of small-scale sediment processes. *Cont. Shelf Res.,* **22,** 603–632, doi:10.1016/S0278-4343(01)00101-7.

——, and M. J. Buckingham, 2004: Measurements of scattering by suspensions of irregularly shaped sand particles and comparison with a single parameter modified sphere model. *J. Acoust. Soc. Amer.,* **116,** 2876–2899, doi:10.1121/1.1808458.

Vikram, C. S., 1992: *Particle Field Holography.* Cambridge University Press, 265 pp.

Zhang, X., R. H. Stavn, A. U. Falster, D. Gray, and R. W. Gould Jr., 2014: New insight into particulate mineral and organic matter in coastal ocean waters through optical inversion. *Estuar. Coast. Shelf Sci.,* **149,** 1–12, doi:10.1016/j.ecss.2014.06.003.